Ore Geology Reviews 144 (2022) 104863

Contents lists available at ScienceDirect

Ore Geology Reviews

journal homepage: www.elsevier.com/locate/oregeorev

# Exploring the Sn–W metallogenic potential of Late Jurassic Ganfang-Guyangzhai granite suite, South China: Zircon and apatite geochemistry

Di Wang [a,*], Xiao-Lei Wang [a], Yue Cai [b,c], Jun-Yong Li [a], De-Hong Du [a], Xu-Jie Shu [d]

[a] State Key Laboratory for Mineral Deposits Research, School of Earth Sciences and Engineering, Nanjing University, Nanjing 210023, China
[b] State Key Laboratory of Palaeobiology and Stratigraphy, Nanjing Institute of Geology and Palaeontology and Center for Excellence in Life and Paleoenvironment, Chinese Academy of Sciences, Nanjing 210008, China
[c] Lamont-Doherty Earth Observatory of Columbia University, Palisades, NY 10964, USA
[d] School of Geographic Science, Nantong University, Nantong 226019, China

ARTICLE INFO

*Keywords:*
Late Jurassic granitoids
Metallogenic potential
Oxygen fugacity
Halogens
Zircon
Apatite

ABSTRACT

Many Late Mesozoic granitoids in South China are associated with the mineralization of tungsten and tin metals. Ore deposits associated with granitoids are key sources of a number of economically important metals, for instance of W and Sn. The significant controls on magma metal fertility are magmatic sources, degrees of differentiation, oxygen fugacities, and halogen contents. Investigating the factors and their metallogenic potential is essential for future exploration. To this end, this study presents new zircon and apatite data for the Late Jurassic *ca.* 145 Ma Ganfang-Guyangzhai granite [GF–GYZ] suite and nearby coeval Shiqiao [SQ] granitoid intrusion near the giant Dahutang tungsten ore deposit. We explore the metallogenic potential in terms of the studies on oxygen fugacity and halogens in melts. These granitoids have similar zircon $\delta^{18}O$ values (SQ: 8.39‰–9.74‰; GF–GYZ: 8.70‰–10.7‰). However, SQ granitoids are more oxidized than GF–GYZ granitoids, with zircon log$fO_2$ values of −18.5 to −8.1 and −24.5 to −16.8, respectively. Apatite grains in these granitoids all have high F (>1.7 wt%) and low Cl (<0.05 wt%) concentrations, yielding extremely low Cl/F ratios (<0.021), which are within the range for tungsten-bearing granitoids worldwide (Cl < 0.5 wt%, Cl/F < 0.02). Furthermore, the more evolved GF–GYZ granitoids show relatively high F (2.26–2.75 wt%) concentrations, which are more similar to granites directly associated with the Dahutang tungsten ore deposit in terms of their magmatic sources, degrees of differentiation, oxygen fugacities, and halogen contents. These geochemical similarities suggest that the GF–GYZ granite intrusions also have significant metallogenic potential for tin and tungsten deposits.

## 1. Introduction

Critical metals (e.g., tungsten and tin) are vital components for economic growth and the overall functioning of modern society (e.g., Moss et al., 2013; Watari et al., 2020). Owing to the significance of these metals, there is an increasing demand for them. As the largest W reserve (*ca.* 45%) and dominant Sn reserve (11%) of the world (e.g., Zhou et al., 2018), South China is characterized by widespread Late Mesozoic granitic magmatism and associated extensive large-scale mineralization (e.g., Zhou et al., 2006, 2018; Mao et al., 2007; Sun et al., 2012; Huang and Jiang, 2014; Zhao et al., 2017; Xie et al., 2019; Zhang et al., 2020), known as the "Mesozoic metallogenic explosion" (Hua et al., 2005). One of the largest metallogenic events took place during 160–139 Ma, forming W–Sn–Nb–Ta mineralization (Li et al., 2017). These tungsten and tin deposits in South China are generally associated with Mesozoic granitoids (Feng et al., 2012; Mao et al., 2013; Huang and Jiang, 2014). For example, some world-class W deposits (e.g., Dahutang tungsten deposits) were recently discovered in the eastern Jiangnan orogen of northwestern Jiangxi Province, which greatly expanded the known prospective areas for W exploration in South China. In the world, tin and tungsten mineralization are also generally related to evolved granites (e.g., Kempe and Wolf, 2006; Neiva, 2008; Fogliata et al., 2012; Xu et al., 2015; Hulsbosch et al., 2016; Mao et al., 2019; Yuan et al., 2019; Jiang et al., 2020; Lehmann, 2021). Many formation mechanisms have been proposed for tin and tungsten mineralization. These include formation through partial melting of fertile metasedimentary rocks (e.g., Song

* Corresponding author.
*E-mail address:* diwang@nju.edu.cn (D. Wang).

https://doi.org/10.1016/j.oregeorev.2022.104863
Received 2 December 2021; Received in revised form 16 February 2022; Accepted 28 March 2022
Available online 30 March 2022

et al., 2018), fluid–rock interaction (e.g., Lecumberri-Sanchez et al., 2017), variations in oxygen fugacity in magmatic–hydrothermal mineralization (e.g., Li et al., 2017), and differential melting temperatures of the granitic melts (e.g., Yuan et al., 2019; Zhao et al., 2021). In these mechanisms, identifying the specific roles of magma source, oxidation state, and halogen concentration during mineralization associated with granitoids is of great importance (e.g., Li and Audétat, 2012; Lecumberri-Sanchez et al., 2017; Li et al., 2017; Song et al., 2018). Therefore, we conduct an investigation into these factors that can potentially be utilized to evaluate the metallogenic potential of granitoids.

Accessory minerals can provide unique and important records of magma conditions and magmatic evolution, and they can be utilized as pathfinders to prospective areas of granite-hosted mineralization (e.g., Gardiner et al., 2017). Zircon is a common mineral in the continental crust, especially in granitoids. Zircon has been widely used to trace magma sources and elucidate magmatic processes (e.g., Kinny and Maas, 2003; Wang et al., 2013a; Tang et al., 2014). For example, oxygen isotope analysis of zircon, combined with geochronology and Hf isotope analysis, has been pivotal in understanding the evolution of the continental crust (Belousova et al., 2006; Kemp et al., 2007; Wang et al., 2013a). Furthermore, the Ce and Eu anomalies of igneous zircon are used as proxies for redox conditions of magmas (e.g., Ballard et al., 2002; Trail et al., 2011, 2012; Smythe and Brenan, 2016; Loader et al., 2017). Like zircon, apatite is also a prevalent and robust detrital and magmatic accessory mineral (Belousova et al., 2002; Morton and Yaxley, 2007; Bruand et al., 2019). In addition, apatite also incorporates some volatile elements (e.g., F and Cl) into its structure, which can be used to investigate the halogen budgets of magmas and their source regions (Douce and Roden, 2006; Li and Costa, 2020; Li et al., 2021). Therefore, zircon and apatite can be useful for determining the characteristics of mineralizing fluids, melt volatile contents, and oxygen fugacities of magmas, and can provide important information on ore-deposit formation.

The Jiuling composite batholith is one of the largest granitic batholiths in South China and crops out over an area of ~2500 km$^2$ (BGMRJX, 1984). It comprises Neoproterozoic and Late Jurassic granitic intrusions, with the latter hosting the second largest tungsten deposit in China, namely the Dahutang polymetallic W–Cu–Mo deposit, in its northern part (Fig. 1b; Mao et al., 2013; Huang and Jiang, 2014). The associated Jurassic granitoids and ore deposits have been studied extensively (e.g., Huang and Jiang, 2014; Pan et al., 2017; Sun et al., 2018; Fan et al., 2019), making this area suitable for detailed research on the metallogenic potential of granitoids in general. Here we present new zircon U–Pb and O isotopic and trace element data alongside apatite compositional data for three Late Jurassic intrusions in the central Jiuling composite batholith. These data allow determination of the magma sources, nature of magmatic fluids, oxygen fugacity conditions, and halogens of these intrusions. These results provide new insights into the petrogenesis of the Jurassic granitoids and have implications for tin and tungsten deposit exploration.

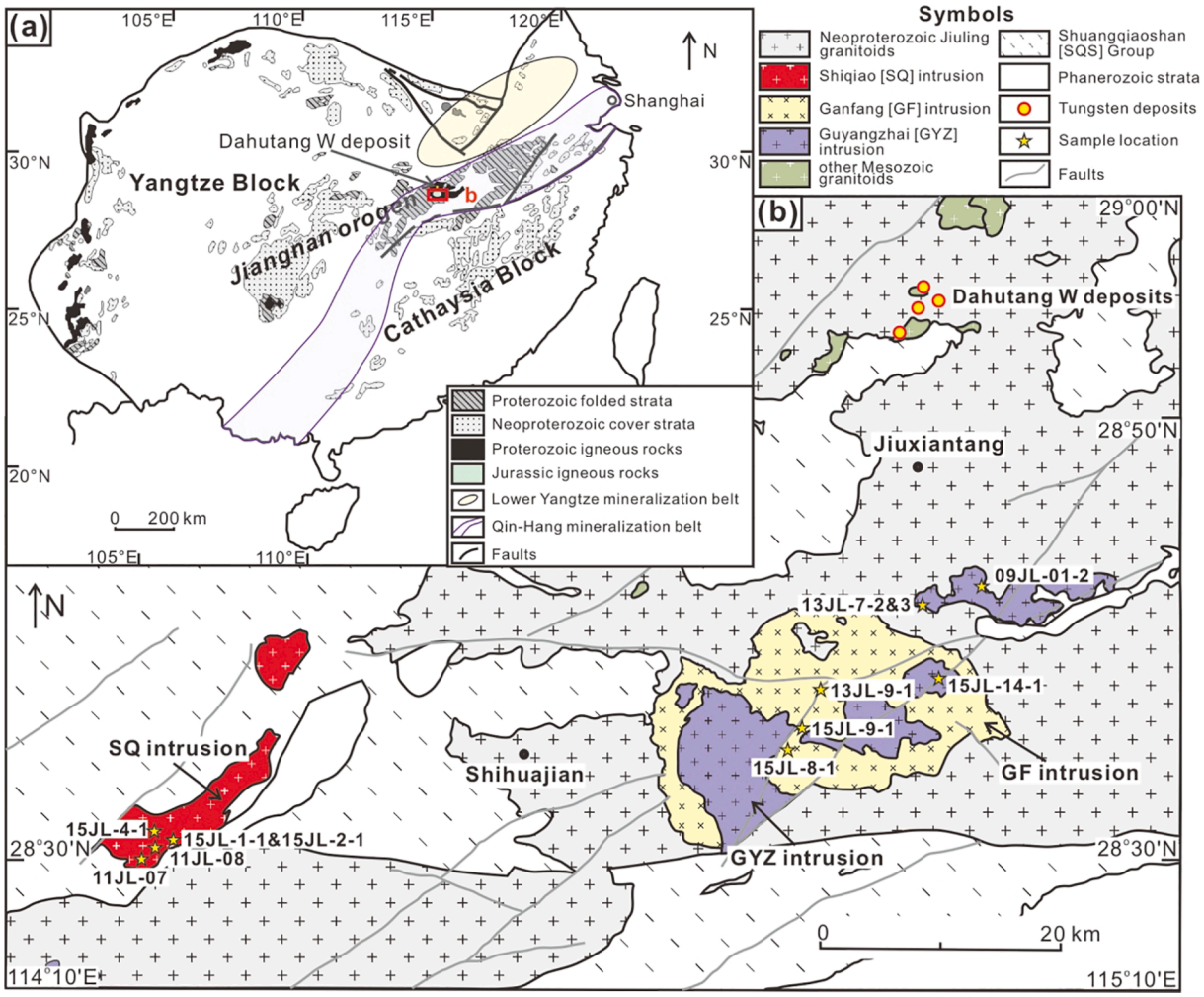


**Fig. 1.** Generalized geological map of (a) South China and (b) the Jurassic intrusions (modified after Wang et al., 2017).

## 2. Geological background

The South China Block is divided by the Jiangnan Orogen into the Cathaysia Block to the southeast and the Yangtze Block to the northwest (Fig. 1a; Wang et al., 2014a). The Jiangnan Orogen is dominated by lower greenschist facies metamorphosed sedimentary strata and Neoproterozoic (960–750 Ma) magmatic rocks that record convergence and rifting on the southeastern margin of the Yangtze Block (e.g., Wang et al., 2007, 2012, 2014; Li et al., 2009; Cawood et al., 2013; Yao et al., 2015, 2019). The metasedimentary sequences within the orogen are divided by a prominent regional angular unconformity (Wang et al., 2007), and the sequences beneath the unconformity (e.g., the Shuangqiaoshan [SQS] Group in the northern Jiangxi Province) are tightly folded (Wang et al., 2014a and references therein). The SQS Group was mainly deposited between 831 ± 5 and 815 ± 5 Ma (Wang et al., 2013b; Li et al., 2016) and is dominated by slate, siltstone, and sandstone that gradually coarsen upwards. The Jiuling composite batholith intrudes the SQS Group (BGMRJX, 1984).

The Jiuling composite batholith consists of a few Neoproterozoic intrusions which are intruded by several Late Jurassic granitic intrusions. The Neoproterozoic Jiuling batholith formed at *ca.* 820 Ma. However, the Jurassic granitic intrusions were emplaced at 148–144 Ma (Wang et al., 2013a, 2014, 2017; Zhao et al., 2013). Among them, the dominant Late Jurassic intrusions can be divided into two sets based on the field relationship following Wang et al. (2017), including the set-1 Shiqiao [SQ] intrusion and the set-2 Ganfang–Guyangzhai [GF–GYZ] intrusive suites (Fig. 1b). Both set-1 and set-2 granitoids intruded the folded metasedimentary rocks (i.e., the SQS Group) and the Neoproterozoic Jiuling composite batholith, respectively. The set-1 SQ granites are gray with massive structures and granular textures. The ~75 km$^2$ set-1 SQ intrusion is dominated by a fine-grained granodiorite phase (Fig. 2) characterized by 40%–60% plagioclase, 20%–30% quartz, 10%–15% biotite, and 10%–15% K-feldspar. Accessory minerals apatite and zircon are present as inclusions in biotite and quartz. The set-2 GF–GYZ intrusive suites, located to *ca.* 30 km east of the set-1 SQ intrusion, are yellowish and gray with massive structures. In the intrusive suites, the set-2 GF intrusion was intruded by the set-2 GYZ intrusion. The ~153 km$^2$ set-2 GF intrusion exhibits porphyritic textures with K-feldspar and quartz megacrysts up to 5–15 mm, and consists of fine- to coarse-grained muscovite and two-mica granites (Fig. 2) that contain 30%–40% K-feldspar, 25%–35% quartz, 15%–25% plagioclase, 5%–15% muscovite, and 0%–10% biotite with accessory zircon and apatite present as inclusions within quartz, plagioclase, and K-feldspar. The ~180 km$^2$ set-2 GYZ intrusion also exhibits porphyritic textures and the predominant megacrysts are K-feldspar with sizes up to 5–10 mm, which are slightly different from those in the set-2 GF intrusion. The set-2 GYZ intrusion consists of fine- to medium-grained two-mica granites (Fig. 2) that contain 30%–45% K-feldspar, 25%–30% quartz, 15%–25% plagioclase, 5%–15% biotite, and 5%–15% muscovite with accessory apatite and zircon present as inclusions within biotite and muscovite.

The recently discovered Dahutang tungsten deposit is located in the northern part of the Jiuling composite batholith (Fig. 1b) and has a total reserve of ~2.0 million tons of $WO_3$, representing one of the largest known tungsten deposits (e.g., Mao et al., 2013); the major ore types are disseminated veinlets, large wolframite-bearing quartz veins, and hydrothermal breccias (e.g., Mao et al., 2013; Song et al., 2018). The


**Fig. 2.** Field photographs and photomicrographs of representative samples from the Late Jurassic granitoids: (a–b) granodiorite (sample 15JL-2-1) from the set-1 SQ intrusion; (c–d) muscovite granite (15JL-9-2) from the set-2 GF intrusion; (e–f) two-mica granite (13JL-6-2) from the set-2 GYZ intrusion. Pl, plagioclase; Kfs, K-feldspar; Bt, biotite; Ms, muscovite; Qtz, quartz.

tungsten mineralization in the deposit occurs close to the intrusive contacts of the Jurassic granitoids (i.e., the Dahutang granitoids). The Dahutang granitoids are adjacent to the two sets of studied Jurassic granitoids but have no direct visible contact with them. The Dahutang granitoids have similar mineral assemblages as the set-2 GF and GYZ granitoids and are composed of two-mica and muscovite granites (Zhao et al., 2017), which formed at 151–142 Ma (e.g., Huang and Jiang, 2014; Pan et al., 2017; Wei et al., 2018).

## 3. Analytical methods

Zircon grains were separated from crushed samples using conventional heavy liquid and magnetic techniques. Transmitted and reflected light microscopy and cathodoluminescence (CL) imaging were used to avoid micro-inclusions and micro-cracks during U–Pb and O isotope and trace-elemental analyses.

Zircon oxygen isotopes and some U–Pb ages were measured using a CAMECA IMS 1280-HR instrument at the State Key Laboratory of Isotope Geochemistry, Guangzhou Institute of Geochemistry, Chinese Academy of Sciences, Guangzhou, China. Details of the analytical procedures used are given in Yang et al. (2018) and Liu et al. (2015). The internal precision of single analyses was generally better than ±0.2‰. Due to the high U concentrations of zircon, a "high-U matrix effect" resulted in anomalously old and discordant SIMS U–Pb ages (Li et al., 2010; White and Ireland, 2012; Wang et al., 2014). The other zircon U–Pb ages and trace-element concentrations were measured using an Agilent 7500a laser ablation-inductively coupled plasma-mass spectrometry (ICP–MS) instrument attached to a New Wave 213 nm LA system at the State Key Laboratory for Mineral Deposits Research, Nanjing University (MiDeR-NJU), Nanjing, China, following the procedures in Wang et al. (2007). Some zircon trace-element concentrations were determined using a Thermo Xeries 2 ICP–MS instrument attached to an nm ArF Excimer LA system at the Analysis and Testing Research Center of Shandong Bureau, China Metallurgical Geology Bureau, Jinan, China. In order to determine the trace-element concentrations of zircon, counts for $^{29}$Si, $^{49}$Ti, $^{139}$La, $^{140}$Ce, $^{141}$Pr, $^{142}$Nd, $^{152}$Sm, $^{153}$Eu, $^{158}$Gd, $^{159}$Tb, $^{164}$Dy, $^{165}$Ho, $^{166}$Er, $^{169}$Tm, $^{172}$Yb, and $^{175}$Lu were collected. Laser ablation beams were 25 or 35 μm in diameter, depending on the size of the zircon grains.

Back-scattered electron (BSE) images of apatite were undertaken by electron probe microanalysis (EPMA) employing a JEOL JXA-8100 instrument at the MiDeR-NJU. BSE images were obtained with an accelerating voltage of 10 kV and a working distance of 6.8 mm. Major-element compositions were also determined using the instrument at the MiDeR-NJU. The instrument was operated in wavelength dispersive mode with a 15 kV accelerating voltage and a 20 nA beam current. Element peaks and backgrounds were measured for all elements with 20 s peak counting times, except for F, La and Ce (10 s peak and 5 s background counting times). F and Cl were analyzed first to reduce the effect of halogen migration. Natural and synthetic standards were used for calibration, including norbergite for F, $Ba_5(PO_4)_3Cl$ for Cl, apatite for P and Ca, monazite for La and Ce, and hornblende for Na, Si, Mg, and Fe. Detection limits are better than 0.02 wt% for most elements, apart from F (0.1 wt%). All EPMA data were automatically reduced using the ZAF correction program, and the method of Ketcham (2015) was used to calculate the chemical formula for apatite, removing uncertainties from the stoichiometric calculations involved (up to 4%). Previous studies have suggested that quantitative analysis of halogens in apatite by EMPA may be affected by crystallographic orientation and electron beam sensitivity (e.g., Stormer et al., 1993; Marks et al., 2012). Most of the crystals in thin sections used in our study were analyzed with their c-axes not parallel to the direction of the electron beam, so F migration during analysis should be minimal (Stormer et al., 1993; Goldoff et al., 2012; Stock et al., 2015).

## 4. Results

### 4.1. Zircon U–Pb dating

All of the zircon grains analyzed during this study are euhedral and 40–250 μm long. The corresponding dating results are presented in the supplementary Tables S1 and S2. The two sets of Late Jurassic granitoids contain zircon with different characteristics visible during CL imaging (Fig. 3). Set-1 granitoid have clear oscillatory zoning in zircon that is indicative of a magmatic origin. In comparison, set-2 granitoids usually contain zircon grains with core–rim structures where the cores contain oscillatory zonation that appears bright CL intensity, with the surrounding rims appearing dark. Some zircon grains have multiple growth stages with corroded crystal outlines. The cores usually have round shapes. The rims of the set-2 granitoids are characterized by homogeneous dark-CL zircon domains. These dark-CL zircon domains contain high and variable Th (10–2000 ppm) and U (generally $>$ 2000 ppm) concentrations which yield low Th/U ratios (typically $<$ 0.2).

LA–ICP–MS or SIMS zircon ages are used to distinguish magmatic vs. inherited zircon. All the results plot on the concordia line (Fig. 4). The youngest spot analyses from set-1 and set-2 granitoids, including the dark-CL rim domains from set-2, yield weighted mean $^{206}$Pb/$^{238}$U ages from 152.4 ± 3.3 (n = 13; MSWD = 3.9) to 143.9 ± 1.7 Ma (n = 11, MSWD = 0.50). It is noted that two samples (13JL-9-1 and 09JL-01-2) only give one or two spot analyses at the crystallization age but more data for the inherited Neoproterozoic cores (Fig. 4c, f). Nonetheless, the spread of the weighted mean ages, the magmatic duration (timescale) could not be precisely distinguished because of the age uncertainty and loose constraints on the date concentrations (Fig. 4a-c, f). Except the two aforementioned samples, there are few analyses at the younger cluster for 13JL-9-1 (Fig. 4b) while the younger analyses of 11JL-07 show a spread on the Concordia line in a small range (Fig. 4a) which may include antecrysts and autocrysts. In this regard, the results of 13JL-7-2 and 13JL-7-3 are likely more representative of the emplacement ages (close to 145 Ma) of the Jurassic intrusions, which are broadly consistent with previously reported ages (Wang et al., 2017). The remaining spot analyses of captured/inherited zircon grains yield older $^{206}$Pb/$^{238}$U ages from 901 ± 7 Ma to 521 ± 13 Ma that cluster around 800 Ma (Fig. 4). These Neoproterozoic ages are overall consistent with the detrital zircon age of the SQS Group and the crystallization age of the Jiuling composite batholith.

### 4.2. Zircon O isotopic compositions

Magmatic zircon grains from set-1 SQ intrusion granitoids (sample 11JL-07) yield $\delta^{18}$O values from 8.39‰ to 9.74‰ (Fig. 5), while the inherited/captured grains/domains exhibit similar but slightly higher $\delta^{18}$O values from 8.53‰ to 9.92‰ (Table S3). These contrasting core-rim oxygen isotopic compositions is evident in Fig. 5c.

The Neoproterozoic bright-CL inherited/captured zircon domains from set-2 GF granitoids (sample 13JL-9-1) exhibit relatively large variations of $\delta^{18}$O values from 6.27‰ to 10.3‰ (Table S3, Fig. 5). In contrast, the inherited/captured zircon domains from set-2 GYZ granitoids (samples 09JL-01-2) have a limited range of $\delta^{18}$O values from 7.46‰ to 10.4‰ (mostly from 8.57‰ to 10.4‰) (Table S3; Fig. 5), which are consistent with the dark-CL magmatic rims from set-2 GYZ granitoids which show a narrow range of $\delta^{18}$O values (8.70‰–10.7‰) (Table S3). Generally, most of the magmatic rims have lower $\delta^{18}$O values than the cores, although a few rims exhibit the opposite relationship (e.g., core 09JL-1-2# 1-1 and rim #1-2) (Fig. 5c).

In summary, zircon rims have similar oxygen isotopic compositions to the cores, especially in set-2 granitoids, which demonstrates O isotopic homogeneity in these different domains.

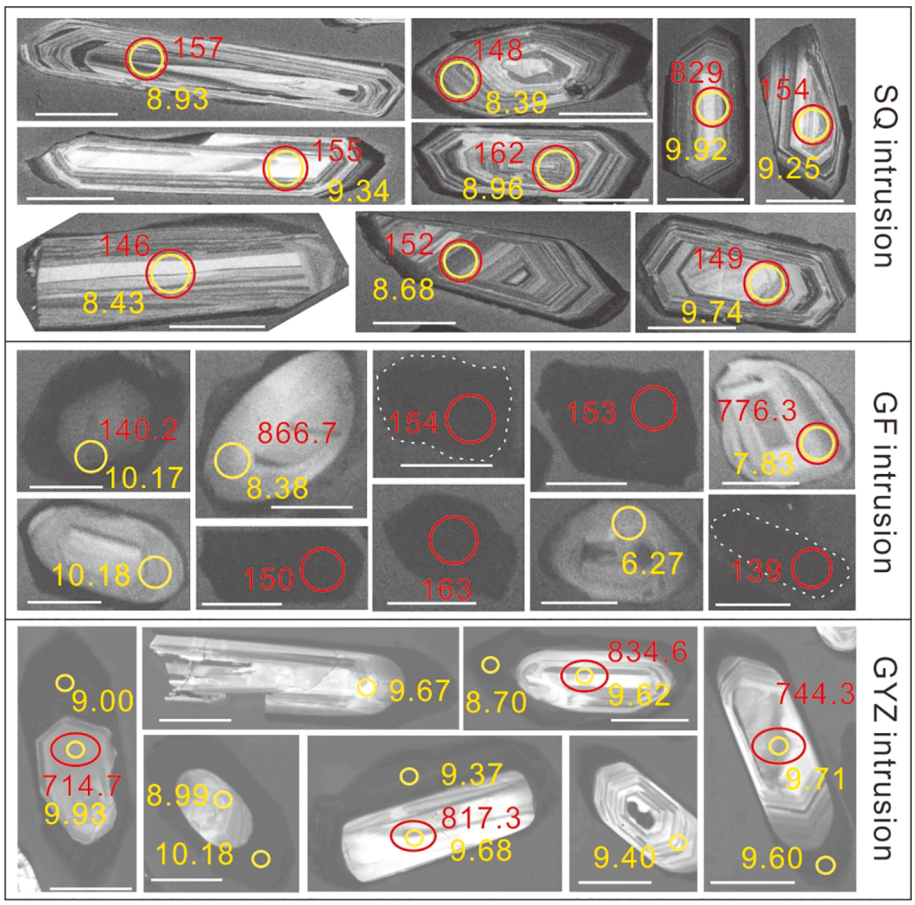


**Fig. 3.** Representative CL images showing the internal structure and morphology of the zircon analyzed in this study. Red circles indicate sites for U–Pb analyses and yellow circles indicate the corresponding sites for zircon oxygen isotope analyses; the U–Pb ages and $\delta^{18}O$ values for each analysis are shown on the figure. The scale bar is 50 μm. (For interpretation of the references to colour in this figure legend, the reader is referred to the web version of this article.)

### 4.3. Zircon trace-element concentrations

The trace element concentrations of the zircon grains analyzed during this study are provided in Table S4. The total rare earth elements (REE) concentrations of zircon grains from set-1 intrusion range from 506 to 1416 ppm (average of 1014 ppm). They have convex-upward chondrite-normalized REE patterns (Fig. S1), and are characterized by LREEs depletion and HREEs enrichment, with positive Ce anomalies ($Ce/Ce^* = 8.4–152$, generally $< 90$) and commonly weak to moderately negative Eu anomalies, all of which are characteristic of magmatic zircon (Hoskin and Schaltegger, 2003), where $Ce^* = (Nd_N)^2/Sm_N$, $Eu^* = 1/2[(Sm)_N+(Gd)_N]$ and subscript N denotes normalization to chondrite-normalized values. However, the dark-CL zircon domains from the set-2 GYZ intrusion have higher total REE concentrations with 3172–6190 ppm for sample 13JL-7-2 and 3356–5122 ppm for sample 13JL-7-3. These dark-CL zircon domains have relatively flat LREE patterns with low $(Sm/La)_N$ ratios (0.35–100.8, generally $< 5$) and are more enriched in HREEs than normal magmatic rims (Fig. S1). These dark-CL domains have strong negative Eu anomalies and moderate/mild positive Ce anomalies ($Ce/Ce^* = 1.25–4.13$, generally $< 2.0$). They also appear murky brown during optical microscopy. CL imaging shows that they have 20–50 mm thick mantles surrounding their cores (Fig. 3). All of these features suggest that zircon formed from magmatic fluids. The bright-CL zircon domains from set-2 intrusions are similar to set-1 zircon grains in that they have low total REE concentrations (207–2245 ppm for sample 13JL-7-2 and 1079–3625 ppm for sample 13JL-7-3) but contrasts with the dark-CL domains in that they are depleted in LREEs with slightly positive Ce anomalies ($Ce/Ce^* = 0.61–5.99$, generally $>$ 2.0).

Zircon Ti concentrations are mostly in the range of 3.17–18.6 ppm for the set-1 zircon grains, 8.86–27.0 ppm for the set-2 dark-CL zircon domains, and 0.86–24.2 ppm for the set-2 bright-CL domains. Titanium-in-zircon thermometry has been used to estimate the temperatures of formation of natural zircon (e.g., Watson and Harrison, 2005; Watson et al., 2006; Harrison et al., 2007; Ferry and Watson, 2007). Apparent temperatures for zircon crystallization ($T_{Ti\text{-}in\text{-}zrc}$) were calculated using the Ti-in-zircon thermometer of Watson et al. (2006), assuming the $\alpha_{TiO2} = 0.7$. Magmatic zircon domains from the set-1 intrusion yield temperatures of 671 °C–839 °C. The Jurassic dark-CL domains of zircon from the set-2 granitoids yield temperatures of 762 °C–882 °C, and the bright-CL domains yield temperatures of 576 °C–869 °C (commonly 766 °C–869 °C).

### 4.4. Apatite compositions

The compositions of representative apatite from the set-1 and set-2 granitoids are given in Table S5. These apatite grains appear homogeneous in BSE images (Fig. S2) and contain high F (>1.72 wt%) and low Cl (<0.05 wt%) concentrations. In general, set-1 apatite contains lower F (1.72–2.48 wt%) and higher $FeO^T$ (0.09–0.59 wt%) contents than the apatite within the set-2 intrusions (2.26–2.75 wt% F and 0.09–0.31 wt% $FeO^T$). Apatite $H_2O$ contents were calculated stoichiometrically using EPMA data and the results range from 1.05 to 1.78 wt% within set-1 granitoids, which is higher than the concentrations determined for the set-2 granitoids (0.81–1.30 wt%). The apatite within the set-1 intrusions also has more restricted variations in MnO contents (0.26–0.64 wt%) than that within the set-2 intrusions (MnO of 0.21–0.25 wt% in the GYZ intrusion and 0.82–2.47 wt% in the GF intrusion). The atomic

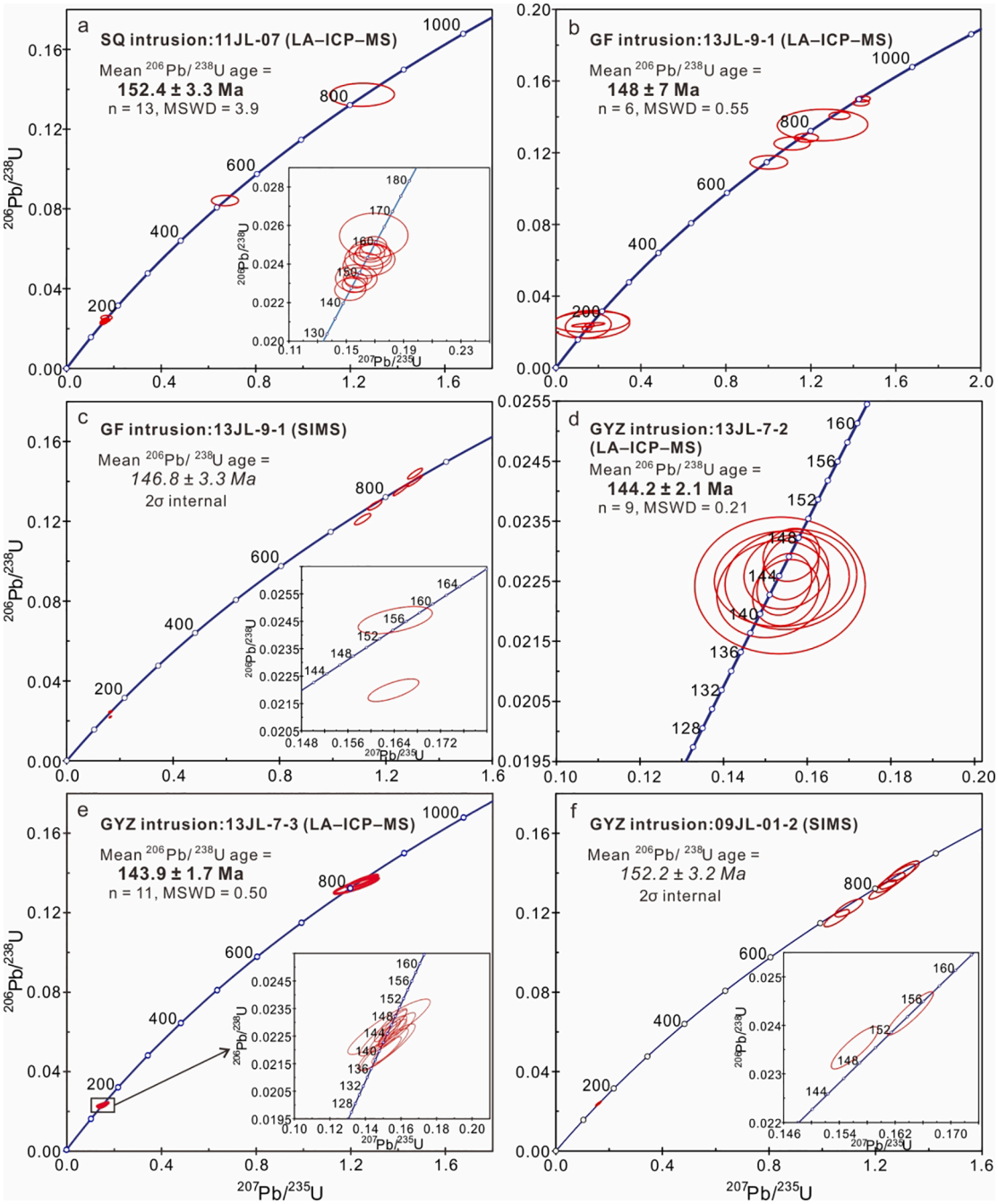


**Fig. 4.** Zircon LA–ICP–MS U–Pb concordia diagrams for the Late Jurassic granitoids in the Jiuling composite batholith.

proportions of F, Cl and OH within apatite from set-1 and set-2 granitoids are indicative of F–OH apatite.

Apatite crystallization temperatures were determined using the empirical apatite saturation temperature (AST) equation for metaluminous systems outlined by Harrison and Watson (1984). $Al_2O_3$ contents are also known to affect AST values in addition to variations in $P_2O_5$ and $SiO_2$ contents (Bea et al., 1992), which led Bea et al. (1992) to propose a modified formula for peraluminous rocks (A/CNK > 1). However, the approach outlined by Bea et al. (1992) means that peraluminous samples with A/CNK values of >1.38 yield higher calculated $P_2O_5$ contents that are clearly different from the correct values. As such, we used only granitoid samples with A/CNK < 1.38 to calculate AST values, thus yielding temperatures of 856 °C for set-1 SQ granitoids, 787–868 °C for set-2 GYZ granitoids, and 830–915 °C for the set-2 GF granitoids.

## 5. Discussion

### 5.1. Oxygen fugacity of the Late Jurassic granitoids

In order to explore the oxygen fugacity of Jurassic magmas, it is necessary to verify the origin of the observed dark-CL zircon domains. Five lines of evidence support a magmatic fluid origin for these domains: (1) Jurassic zircon domains within the set-2 intrusion appear murky brown during optical microscopy and homogenous and dark during CL imaging. Some of these dark-CL domains appear as 20–50 mm thick mantles around bright-CL cores, features that are similar to hydrothermal zircon grains formed from magmatic fluids (Hoskin, 2005). (2) The dark domains have high La concentrations (generally 1.54–75.7 ppm), low $(Sm/La)_N$ ratios (0.35–100.8, generally < 5), and slightly positive Ce anomalies (Ce/Ce*=1.25–4.13), all of which are indicative of a

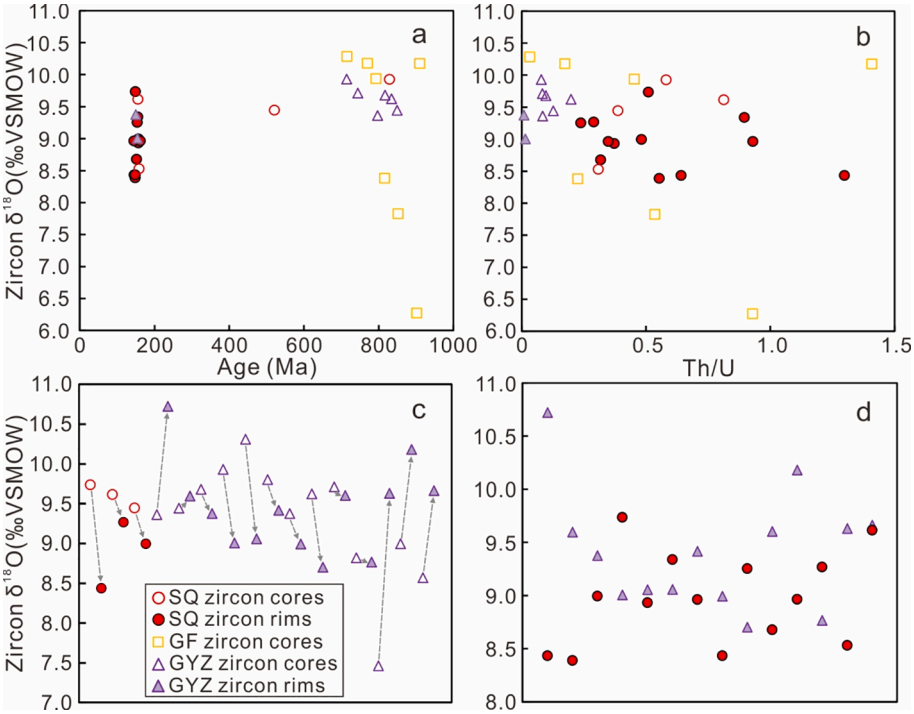


**Fig. 5.** Variations in the $\delta^{18}O$ values of individual zircon from the Jurassic intrusions. (a) $\delta^{18}O$ vs. U–Pb age and (b) Th/U diagrams for zircon cores and rims. (c) Variations in the $\delta^{18}O$ values of individual zircon from the set-1 SQ and set-2 GYZ intrusions. (d) Comparison between black-CL rims within zircon from the set-2 GYZ intrusion and bright-CL rims from the set-1 SQ intrusion. Dashed tie-lines indicate in-situ $\delta^{18}O$ analyses performed on core–rim pairs.

hydrothermal origin (Fig. S1). (3) Post-magmatic hydrothermal zircon generally crystallizes at relatively low temperatures (<500 °C; e.g., Fu et al., 2009; Lei et al., 2016). However, the high $T_{Ti\text{-}in\text{-}zrc}$ temperatures (762 °C–882 °C) of the dark-CL domains preclude a post-magmatic hydrothermal origin but instead indicate a late-stage magmatic–hydrothermal origin. (4) The $\delta^{18}O$ values of set-2 dark-CL zircon domains (8.70‰–10.7‰) are consistent with those of set-2 bright-CL domains (8.57‰–10.4‰), and bright-CL domains of set-1 zircon (8.39‰–9.74‰). These results indicate that these different domains are of the same origin and were not affected by fluids, because high-T water–rock interaction can decrease $\delta^{18}O$ values of magmas dramatically (e.g., Zheng et al., 2007). (5) Variations in the whole-rock compositions of the granitoids, including tetrad effects and K/Rb and Nb/Ta ratios, are indicative of magmatic differentiation and interaction with magmatic fluids (Wang et al., 2017). Therefore, these dark-CL zircon domains are of magmatic fluid origin and possibly formed during differentiation.

Oxygen fugacity ($fO_2$) conditions during magmatism exert significant control on the speciation of multivalent elements, as such the importance of oxygen fugacity conditions as a control on magmatic–hydrothermal mineralization is increasingly recognized (e.g., Richards, 2009, 2015; Mengason et al., 2011; Trail et al., 2012; Li et al., 2017). Many oxybarometers have been proposed, including those that use the composition of biotite (e.g., Richards, 2015) or Ce and Eu anomalies of zircon (e.g., Trail et al., 2012; Smythe and Brenan, 2016; Loader et al., 2017).

The Ce and Eu anomalies of igneous zircon have long been considered to reflect redox conditions in source magmas (Ballard et al., 2002; Trail et al., 2011, 2012; Smythe and Brenan, 2016; Loader et al., 2017). However, these anomalies may also be inherited from the melts from which the zircon crystallized. The partitioning of $Eu^{2+}$ into other minerals, especially plagioclase, which is a common mineral in felsic magmas, introduces uncertainty in this oxybarometer because fractional crystallization of plagioclase generates low Eu/Eu* values in zircon. Although Ce anomalies are also influenced by crystallization of other REE-bearing phases (Loader et al., 2017), the amount of Ce present as $Ce^{4+}$ in terrestrial magmas is thought to be only 0.05%–0.1%, meaning that Ce anomalies are extremely rare (Ballard et al., 2002; Burnham and Berry, 2014). Very few phases preferentially partition Ce over La or Pr. Those that do (e.g., zircon) are typically present in very low abundances, meaning that the crystallization of these minerals does not generate significant Ce anomalies in the residual melt. As a result, Ce anomalies in zircon are relatively robust redox proxies for magmas.

Lattice strain models (Blundy and Wood, 1994) can be used to estimate zircon Ce anomalies using REE (e.g., Nd, Sm, and Gd–Lu; Trail et al., 2012; Qiu et al., 2013), especially considering the refinement of these models (Burnham and Berry, 2012; Smythe and Brenan, 2016; Zou et al., 2019). However, the dark-CL zircon domains analyzed in this study have high La concentrations (generally > 1.0 ppm), which are not characteristic of "clean zircon" (inclusion-free zircon that faithfully records the true zircon REE composition with La < 0.1 ppm; Zou et al., 2019). Moreover, these dark-CL domains have variable LREE and $D_{zircon/whole\text{-}rock}$ (where D is the zircon–melt partition coefficient) values; therefore, their $D_{zircon/whole\text{-}rock}$ values deviate from the lattice strain model, which would yield meaningless oxygen fugacity values. In addition, water contents and chemical compositions of melts are required for the estimation of magmatic oxygen fugacity conditions using cerium zircon–melt partitioning (Smythe and Brenan, 2016). These two melt parameters can be estimated in volcanic systems but are often poorly constrained in intrusions. Owing to complex magmatic processes, such as fractional crystallization, whole-rock geochemical compositions may not fully reflect the compositions of melts from which zircon crystallizes. Moreover, no melt inclusions are present to better constrain water contents in intrusions.

As an alternative, Ce* values may be calculated based on $Ce^* = \sqrt{(La)_N \cdot (Pr)_N}$. However, this approach is still problematic because the concentrations of La and Pr in zircon (10 s–100 s of ppb; Hoskin and Schaltegger, 2003) are too low to be precisely determined by LA–ICP–MS. Instead, this approach may be suitable for dark-CL zircon domains, which contain high LREE concentrations. However, these

domains may contain tiny inclusions of LREE-enriched phases, such as apatite, monazite, and titanite, all of which can yield erroneously high La and Pr concentrations and incorrect estimates of Ce*. Other research suggest that these uncertainties can be avoided by calculating Ce* using $(Nd_N)^2/Sm_N$ (Loader et al., 2017). We adopt the latter method in this study. The $fO_2$ values of zircon from the studied intrusions are shown in Fig. 5. These data indicate that most of the zircon from the set-2 granitoids yield lower $fO_2$ values than those from the set-1 granitoids. The dark-CL domains in zircon from the set-2 granitoids have $\log fO_2$ values from −24.5 to −16.8 (i.e., FMQ −7.47 to −2.94), whereas zircon from the set-1 granitoids has $\log fO_2$ values from −18.5 to −8.1 (i.e., FMQ +0.91 to +6.74), which indicates that set-2 granitoid magmas were more reduced. Based on the different Nd isotopes and evolution paths constrained by energy-constrained assimilation–fractional crystallization (EC-AFC) model (Wang et al., 2017), the sources of two sets of granitoids should be different. More specifically, the set-1 granitoids were formed by partial melting of Proterozoic psammitic sedimentary rocks (e.g., greywackes); in contrast, the set-2 granitoids were generated by partial melting of pelites. The low $\log fO_2$ values of the set-1 SQ granitoids can be ascribed to the presence of reduced organic carbon in their metasedimentary source (e.g., Bucholz et al., 2018).

### 5.2. Melt halogens identified by the analysis of magmatic apatite

Halogens (i.e., fluorine and chlorine) are often involved in a range of magmatic to hydrothermal processes and can control the viscosity of melts and the partitioning of metals into fluids (e.g., Coulson et al., 2001; Pyle and Mather, 2009). The structure of magmatic apatite permits the incorporation of several volatile elements (e.g., F and Cl; e.g., Webster and Piccoli, 2015; Li and Costa, 2020). There are several lines of evidence that suggest igneous origins for the apatite grains in the studied granitoids. First, apatite is commonly present as inclusions within some major mineral phases such as quartz, plagioclase, and biotite, indicating that apatite was an early crystallization phase. Second, the BSE images show homogeneous compositions with no compositional zoning. Third, pores or fluid inclusions, such as monazite and xenotime, are absent in our samples, which precludes the possibility of interaction with fluids (e.g., Betkowski et al., 2016), as hydrothermal fluid activity is unlikely to result in such relatively homogeneous textures and few mineral inclusions. Finally, Cl-apatite (>3.5 wt% Cl) is very common in hydrothermal systems (Webster and Piccoli, 2015), as Cl is preferentially partitioned into fluid phases. However, this contrasts with the F–OH composition of the apatite in the study area, again indicating that these apatite grains are igneous in origin. Therefore, the apatite grains likely reflect the halogens of the magmas that formed the granitoids, with apatite from set-2 intrusions containing more F than that from the set-1 intrusion.

Numerous studies have investigated the partitioning of F and Cl between minerals (e.g., apatite) and melts within magmatic systems, and the consensus is that their partitioning behaviors depend on numerous factors, including mineral and melt compositions and temperatures (e.g., Mathez and Webster, 2005; Webster et al., 2009). A thermodynamic model for apatite dependent on these compositions and temperatures (Li and Costa, 2020) can be used to calculate exchange coefficients ($K_D$) for OH–Cl, OH–F and Cl–F within apatite. However, calculating OH values using EPMA based stoichiometric approaches involve large errors due to uncertainties involved in determining elemental concentrations by EPMA and assuming stoichiometric anion sites (e.g., Schettler et al., 2011; Li et al., 2021). As such, we only used the exchange coefficients ($K_D$) for Cl and F. Apatite from set-1 granitoids have more variable Cl/F ratios (0.001–0.021) than those from set-2 granitoids (0–0.014). Melts in equilibrium with apatite in quartz from set-1 granitoids have a higher mole fraction ratio of $\frac{X_{Cl}^{melt}}{X_F^{melt}}$(0.14; where $X_{Cl}^{melt}$and$X_F^{melt}$ are the mole fractions of Cl and F in the melt). In contrast, melts in equilibrium with apatite in set-1 biotite and set-2 quartz and K-feldspar have low $\frac{X_{Cl}^{melt}}{X_F^{melt}}$ values (0–0.09) that lie within a broadly similar range. Apatite in inclusions within quartz from set-2 granitoid melts have $\frac{X_{Cl}^{melt}}{X_F^{melt}}$ values that are lower than those calculated for apatite in quartz from set-1 melts (Table S5). In addition, the overall $\frac{X_{Cl}^{melt}}{X_F^{melt}}$ values (0.02–0.09) for set-2 GF granitic melts are slightly higher than those calculated for set-2 GYZ melts (0–0.04). The extremely low $\frac{X_{Cl}^{melt}}{X_F^{melt}}$ values of these Jurassic granitoids indicate fluorite enrichment in melts, which is an important feature of tin systems (Lehmann, 2021).

### 5.3. Implications for tin and tungsten mineralization

The newly discovered Dahutang deposit in northern Jiangxi Province is one of the largest polymetallic tungsten deposits in the world. It is thought to be related to Late Jurassic granitoids in the northern part of the Jiuling composite batholith (e.g., Mao et al., 2013; Huang and Jiang, 2014). The associated granitoids yield zircon U–Pb ages that range from 151.3 ± 2.8 to 142.7 ± 2.3 Ma (e.g., Huang and Jiang, 2014; Pan et al., 2017; Wei et al., 2018), which is consistent with the timing of emplacement of the set-1 and set-2 Jurassic granitoids (152.4 ± 3.3 to 143.9 ± 1.7 Ma). The set-1 and set-2 intrusions adjacent to the Dahutang tungsten deposit also form part of the northern Jiuling composite batholith. The Dahutang granitoids consist of porphyritic two-mica, fine-grained muscovite, porphyritic two-mica, and fine-grained two-mica granites and granite porphyry dykes (Zhao et al., 2017), which indicates that they are compositionally similar to the Jurassic granitoids but different in texture. As such, the three largest Jurassic intrusions (i.e., the SQ, GYZ, and GF intrusions) can provide insights into the tungsten prospectivity of this area. Several key aspects (i.e., magma sources, fractional crystallization, oxygen fugacity values, and melt halogens) are discussed below, providing insights into the potential for these granitoids to be associated with tungsten mineralization.

Due to the similarities in zircon $\varepsilon_{Hf}(t)$ values and corresponding $T_{DM2}$ ages, the magmas that formed the Late Jurassic granitoids were derived from sedimentary sources (including greywackes and pelites) similar to the underlying SQS Group (Wang et al., 2017). The Dahutang granitoids are also thought to be derived from SQS Group (e.g., Huang and Jiang, 2014). Sedimentary rocks in the SQS Group contain higher concentrations of W, Sn, and Cu (11.8, 21.4, and 231 ppm, respectively; Huang and Jiang, 2014 and references therein) than typical crustal rocks (Rudnick and Gao, 2004). These Jurassic granitoids have very low tungsten concentrations (<6 ppm) and variable tin concentrations (0.31–72.5 ppm) (Wang et al., 2017). Whole-rock tin contents can be used to distinguish tin-producing granites and non-tin granites (e.g., Lehmann, 1990, 2021). Some of the set-2 granitoids have relatively high tin concentrations (>17 ppm), which are located in the northern part of the intrusive suites and could be related to the tin deposits. Generally, Sn contents above 17 ppm are considered protolith with Sn ore potential (e.g., Gardiner et al., 2017). Meanwhile, fluids can extract ore-forming elements and lower their contents in the host rock. Tin in hydrothermal fluids is mainly transported as chloride complexes (mainly $SnCl^-$ and $SnCl_2$) (e.g., Wilson and Eugster, 1990; Lehmann, 2021). In contrast, tungsten is transported as part of an oxyanion ($WO_4^{2-}$) which can be complexed with cations ($Na^+$, $K^+$, or $H^+$) in hydrothermal solutions (Wood and Samson, 2000). Precipitation of tungstate minerals (e.g., scheelite and wolframite) and tin minerals (e.g., cassiterite) leads to low concentrations of W and Sn in the residual magmas. Therefore, despite their low W and Sn contents in some samples, the Jurassic set-2 magmas in this area might still be enriched in these metals, especially Sn. Other factors need to be considered, such as the source rocks, the degrees of fractionation of the magma, their chloride and fluoride contents, and their oxygen fugacity.

Degrees of fractionation is one parameter of particular importance for magmatic metallic enrichment in granite suites (e.g., Lehmann,

2021). Highly fractional crystallization can concentrate metals such as W and Sn within the melt phases of a differentiating magma. Significant fractional crystallization can also lead to exsolution of magmatic–hydrothermal fluids during later stages of magmatism. Such magmatic fluids are thought to be primary carriers of many of the components needed to form mineral deposits, including metals and their ligands (e.g., Wood and Samson, 2000; Zhao et al., 2022). For example, Sn prefer to partition into fluid phase during the exsolution of fluid from granitic magma (Zhao et al., 2022). The set-2 GF–GYZ granitoids in our study and Dahutang granitoids are all differentiated, due to the presence of albite (Huang and Jiang, 2014; Wang et al., 2017). Moreover, the dark-CL zircon domains likely crystallized from magmatic fluids during late stage magmatism (as discussed in section 5.1). Dark-CL zircon are only present in set-2 granitoids, and these zircon domains are similar to that of the Dahutang granitoids with relatively flat LREE patterns and high U concentrations. Therefore, the set-2 and Dahutang magmas were both highly differentiated and were influenced by magmatic–hydrothermal fluid processes. Thus, the set-2 granitoids have high tin and tungsten metallogenic potential. Meanwhile, the set-1 SQ intrusion is dominated by granodiorite with low degree of fractional crystallization due to absence of albite and dark-CL zircon domains. According to Yuan et al. (2018), the granitic intrusion with low degree of fractionation has low potential to form W–Sn deposits. Therefore, set-1 SQ granitoids may have low Sn–W ore potential.

Redox conditions (i.e., oxygen fugacity) also play a pivotal role in determining the metallogenic properties of plutonic bodies (e.g., Miles et al., 2014). Zhang et al. (2016) suggested that oxygen fugacity could control the relative efficiency of the movement of metals from magmas into associated ore-forming fluids. In addition, Cu and Mo mineralization is usually associated with oxidized magmas and environments whereas Sn mineralization is usually linked with low oxygen fugacity conditions (e.g., Blevin and Chappell, 1992; Ballard et al., 2002; Zhang et al., 2016). In reduced melts ($\log fO_2$ < FMQ + 2.5), tin is largely present as $Sn^{2+}$-chloride complexes, which is highly mobile in melts (e.g., Wang et al., 2017). Meanwhile, W behaves as an incompatible element under different redox states (Mengason et al., 2011; Li et al., 2013). This means that W mineralization can be developed under low $fO_2$ conditions in association with Sn mineralization, and also under relatively high $fO_2$ conditions without Sn (Li et al., 2017). Set-1 magmas are relatively oxidized with zircon $\log fO_2$ values (−18.5 to −8.1; Fig. 6). In contrast, set-2 magmas are more reduced with lower zircon $\log fO_2$ values (−24.5 to −16.8; Fig. 6) that are similar to those determined for Dahutang magmas (generally below FMQ; Sun et al., 2018; Wei et al., 2018). These similarities in oxygen fugacity between set-2 and Dahutang granitoids suggests that the reduced set-2 magmas are potential exploration targets for Sn-(W) mineralization.

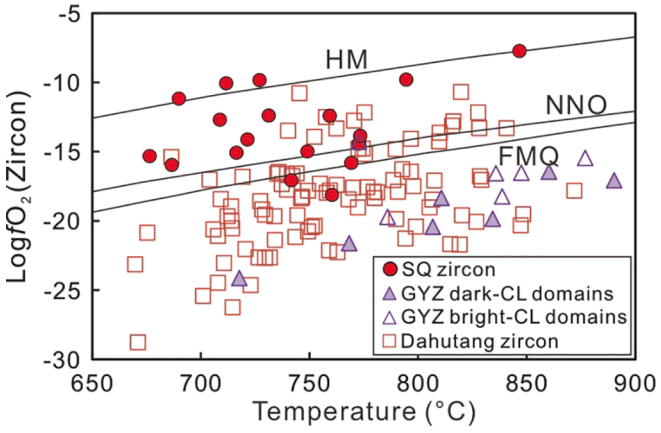


**Fig. 6.** Zircon oxygen fugacity ($\log fO_2$) vs. $T_{Ti\text{-}in\text{-}zrc}$ temperatures of the Jurassic magmas. QFM = quartz–fayalite–magnetite buffer, NNO = nickel–nickel oxide buffer, and HM = hematite–magnetite buffer. Oxygen fugacity values for zircon from the Dahutang granites are from Wei et al. (2018) and Sun et al. (2018).

Although the transportation of Sn and W within magmatic–hydrothermal fluids do not directly involve halogens, the ratio of Cl and F in magmatic systems is still worth discussing, as it is a key factor in the genesis of Sn and W mineralization (e.g., Webster et al., 2004; Rasmussen and Mortensen, 2013; Zhang et al., 2016). The presence of fluorine depresses the magmatic solidus and prolongs magmatic fractionation, which enhances the likelihood for an evolving magma to achieve Sn saturation and as a result, improves mineralization potential (e.g., Vonopartis et al., 2021). Theoretical modeling also suggests that the presence of $F^-$ may increase both the electronegativity and chemical hardness of fluid phases, both of which would increase the solubility of W and Sn (Vigneresse, 2009). In addition, F and Cl play an important role in facilitating the transfer of hydrothermal metals and enabling ore deposition during magmatic evolution (Sun et al., 2007; Harlov, 2015; Guo et al., 2016; Jiang et al., 2018). Apatite from these Jurassic granitoids has high F (1.7–2.75 wt%) and low Cl (0–0.05 wt%) concentrations and low Cl/F ratios (0–0.021). These characteristics are indicative of formation from melts with low $\frac{X_{Cl}^{melt}}{X_{F}^{melt}}$ values (0–0.14; but mostly < 0.09). These conditions are generally related to melts with high metal solubilities, indicating that they could contain high concentrations of metals such as W and Sn. The apatite from the Dahutang granitoids associated with the tungsten deposit (Han et al., 2016) has similar halogen abundances and ratios to the granitoids. Specifically, these minerals contain high F concentrations (1.21–3.10 wt%) and low Cl concentrations (<0.03 wt%) and Cl/F ratios (0–0.023), which are indicative of formation from melts with low $\frac{X_{Cl}^{melt}}{X_{F}^{melt}}$ values (0–0.15, generally 0–0.06). Therefore, the Jurassic granitoids may be associated with tin and tungsten mineralization.

In summary, the studied Jurassic granitoids, especially the set-2 granitoids, show close affinities to the Dahutang granitoids, including their spatial and temporal distributions, magma sources, magmatic fluids, oxygen fugacity, and halogens in melts. These evidences suggest that they are potential exploration targets for metallic (e.g., Sn and W) mineralization.

In order to find more evidence of possible mineralization, we also collected compositional data from apatite in ore-bearing and barren granitoids around the world. This compilation of geochemical data indicates that apatite associated with ore-bearing and barren granitoids has distinct features in terms of halogen concentrations and ratios (Fig. 7), albeit with some overlap between apatite from barren and fertile granitoids. More specifically, apatite from barren granitoids predominantly has high F (>2.3 wt%) and Cl (>0.05 wt%) concentrations and Cl/F ratios (>0.02). In particular, apatite in granitoids related to copper and molybdenum deposits defines a wide field with variable F concentrations. However, apatite in granitoids related to tin deposits has high F (>2.3 wt%) concentrations but variable Cl (0.01–0.2 wt%) concentrations Cl/F ratios (0.003–0.05). Moreover, apatite in granitoids associated with tungsten mineralization is compositionally distinct, with relatively low Cl concentrations (<0.05 wt%) and Cl/F ratios (<0.02). In our study, apatite from the set-1 and set-2 granitoids has low Cl concentrations (0–0.05 wt%) and Cl/F ratios (0–0.021), and variable F concentrations (1.7–2.8 wt%), and plot within the range of apatite associated with tin and tungsten mineralization. This is consistent with set-1 and set-2 granitoids being considered highly promising for exploration for tin and tungsten mineralization.

Many tungsten, niobium, tantalum, and polymetallic deposits are associated with contemporaneous granitoids. These include the Dajishan granites (Wu et al., 2017), the Laiziling granite (Xie et al., 2018), the Limu granite (Huang et al., 2020), and the Jiulongnao granitic complex (Guo et al., 2018) in South China, the Cornubian granitic batholith in England (Simons et al., 2017), and the Krásno–Horní Slavkov granite in the Czech Republic (René and Škoda,

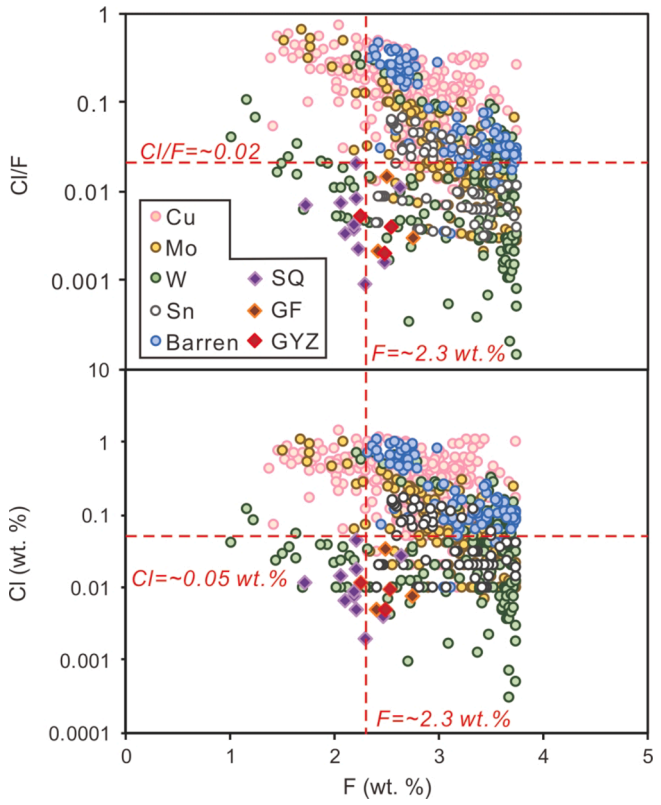


**Fig. 7.** Discrimination diagrams for apatite in ore-bearing and barren granitoids worldwide. The majority of apatite in barren granitoids has high F concentrations (>2.3 wt%), Cl concentrations (>0.05 wt%) and Cl/F ratios (>0.02). The apatite fields of granitoids associated with W, Sn, Cu, and Mo mineralization and barren granitoids are from Rasmussen and Mortensen (2013), Ding et al. (2015), Pan et al. (2016), Gebru (2017), Zhong et al. (2018), Adlakha et al. (2018), Azadbakht et al. (2018), Song et al. (2018), Yang et al. (2018), Duan et al. (2019), Qian et al. (2019), Zafar et al. (2019), Jia et al. (2020), Qi et al. (2020), Xing et al. (2020), Chen et al., (2021) and Song et al. (2021).

2011). Such W-Sn-Nb-Ta mineralization displays distinct vertical zonation in South China (e.g., Jiang et al., 2020). Our study area also contains Nb–Ta mineralization associated with the Jurassic Yifeng granite (Xie et al., 2019), again highlighting the exploration potential of the Late Jurassic granitoids, particularly the set-2 granitoids.

## 6. Conclusions

This study presents new zircon LA–ICP–MS and SIMS U–Pb geochronological, mineralogical, and in-situ isotopic data for Late Jurassic granitoids that reveal the magmatic sources of these intrusions and the redox conditions of these magmas. The set-1 SQ granitoids are mainly granodiorite that formed at *ca.* 152 Ma, whereas the set-2 GF and GYZ granitoids are dominated by two-mica and muscovite granites that formed at 152–144 Ma. The set-2 granitoids contain abundant dark-CL zircon grains that likely crystallized from magmatic fluids during the later stages of magmatic evolution. Comparing with the granitoids associated with tin and tungsten deposits in the world, zircon and apatite from these Jurassic granitoids mirror the compositions of their source magmas and share a number of similarities, including magma sources, degree of differentiation, oxygen fugacity conditions, and melt halogens. Our compilation of geochemical apatite data highlights systematic differences between barren and ore-bearing granitoids in terms of F and Cl concentrations and Cl/F ratios, suggesting that these data can be used to identify intrusions that may be associated with mineralization. Apatite grains from the Jurassic granitoids have high F concentrations and low Cl concentrations and Cl/F ratios, which suggest that they plot in the field of apatite associated with tungsten mineralization worldwide. These results suggest that the Jurassic granitoids in the study area, especially the set-2 granitoids, should be considered prospective for tin and tungsten exploration.

## Declaration of Competing Interest

The authors declare that they have no known competing financial interests or personal relationships that could have appeared to influence the work reported in this paper.

## Acknowledgements

This work was substantially supported by the National Natural Science Foundation of China (Grant Nos. 41802051) and the Fundamental Research Funds for the Central Universities of Ministry of Education of China (020614380071). We thank the assistance from G. C. Wang for LA-ICP-MS analyses and X. P. Xia for SIMS analyses.

## Appendix A. Supplementary data

Supplementary data to this article can be found online at https://doi.org/10.1016/j.oregeorev.2022.104863.

## References

Adlakha, E., Hanley, J., Falck, H., Boucher, B., 2018. The origin of mineralizing hydrothermal fluids recorded in apatite chemistry at the Cantung W-Cu skarn deposit, NWT, Canada. Eur. J. Mineral. 30 (6), 1095–1113.
Azadbakht, Z., Lentz, D.R., McFarlane, C.R., 2018. Apatite chemical compositions from Acadian-related granitoids of New Brunswick, Canada: implications for petrogenesis and metallogenesis. Minerals 8 (12), 598.
Ballard, J.R., Palin, M.J., Campbell, I.H., 2002. Relative oxidation states of magmas inferred from Ce (IV)/Ce (III) in zircon: application to porphyry copper deposits of northern Chile. Contrib. Miner. Petrol. 144 (3), 347–364.
Bea, F., Fershtater, G., Corretgé, L.G., 1992. The geochemistry of phosphorus in granite rocks and the effect of aluminium. Lithos 29 (1–2), 43–56.
Belousova, E.A., Griffin, W.L., O'Reilly, S.Y., 2006. Zircon crystal morphology, trace element signatures and Hf isotope composition as a tool for petrogenetic modelling: examples from Eastern Australian granitoids. J. Petrol. 47 (2), 329–353.
Belousova, E.A., Griffin, W.L., O'Reilly, S.Y., Fisher, N.I., 2002. Apatite as an indicator mineral for mineral exploration: trace-element compositions and their relationship to host rock type. J. Geochem. Explor. 76, 45–69.
Betkowski, W.B., Harlov, D.E., Rakovan, J.F., 2016. Hydrothermal mineral replacement reactions for an apatite-monazite assemblage in alkali-rich fluids at 300–600° C and 100 MPa. Am. Mineral. 101 (12), 2620–2637.
BGMRJX (Bureau of Geology and Mineral Resources of Jiangxi Province),, 1984. Regional Geology of Jiangxi Province. Geological Publishing House, Beijing (in Chinese).
Blevin, P.L., Chappell, B.W., 1992. The role of magma sources, oxidation states and fractionation in determining the granite metallogeny of eastern Australia. Trans. Royal Soc. Edinburgh: Earth Sci. 83, 305–316.
Blundy, J., Wood, B., 1994. Prediction of crystal–melt partition coefficients from elastic moduli. Nature 372 (6505), 452–454.
Bruand, E., Storey, C., Fowler, M., Heilimo, E., 2019. Oxygen isotopes in titanite and apatite, and their potential for crustal evolution research. Geochim. Cosmochim. Acta 255, 144–162.
Bucholz, C.E., Stolper, E.M., Eiler, J.M., Breaks, F.W., 2018. A comparison of oxygen fugacities of strongly peraluminous granites across the Archean-Proterozoic boundary. J. Petrol. 59 (11), 2123–2156.
Burnham, A.D., Berry, A.J., 2012. An experimental study of trace element partitioning between zircon and melt as a function of oxygen fugacity. Geochim. Cosmochim. Acta 95, 196–212.
Burnham, A.D., Berry, A.J., 2014. The effect of oxygen fugacity, melt composition, temperature and pressure on the oxidation state of cerium in silicate melts. Chem. Geol. 366, 52–60.
Cawood, P.A., Wang, Y., Xu, Y., Zhao, G., 2013. Locating South China in Rodinia and Gondwana: A fragment of greater India lithosphere? Geology 41, 903–906.
Chen, X.L., Huang, W.T., Chen, L., Zou, S.H., Zhang, J., Li, K.X., Liang, H.Y., 2021. Controlling factors of different Late Cretaceous granitoid-related mineralization between western margin of the Yangtze Block and the neighbor Yidun arc. Ore Geol. Rev. 139, 104554.
Coulson, I.M., Dipple, G.M., Raudsepp, M., 2001. Evolution of HF and HCl activity in magmatic volatiles of gold-mineralized Emerald Lake intrusion, Yukon Territory, Canada. Miner. Deposita 26, 594–606.

Ding, T., Ma, D., Lu, J., Zhang, R., 2015. Apatite in granitoids related to polymetallic mineral deposits in southeastern Hunan Province, Shi-Hang zone, China: implications for petrogenesis and metallogenesis. Ore Geol. Rev. 69, 104–117.
Douce, A.E.P., Roden, M., 2006. Apatite as a probe of halogen and water fugacities in the terrestrial planets. Geochim. Cosmochim. Acta 70 (12), 3173–3196.
Duan, X.X., Chen, B., Sun, K.K., Wang, Z.Q., Yan, X., Zhang, Z., 2019. Accessory mineral chemistry as a monitor of petrogenetic and metallogenetic processes: a comparative study of zircon and apatite from Wushan Cu-and Zhuxiling W (Mo)-mineralization-related granitoids. Ore Geol. Rev. 111, 102940.
Fan, X., Mavrogenes, J., Hou, Z., Zhang, Z., Wu, X., Dai, J., 2019. Petrogenesis and metallogenic significance of multistage granites in Shimensi tungsten polymetallic deposit, Dahutang giant ore field, South China. Lithos 336, 326–344.
Feng, C.Y., Zhang, D.Q., Xiang, X.K., Li, D.X., Qu, H.Y., Liu, J.N., Xiao, H., 2012. Re–Os isotopic dating of molybdenite from the Dahutang tungsten deposit in northwestern Jiangxi Province and its geological implication. Acta Petrologica Sinica 28, 3858–3868 in Chinese with English Abstract.
Ferry, J.M., Watson, E.B., 2007. New thermodynamic models and revised calibrations for the Ti-in-zircon and Zr-in-rutile thermometers. Contrib. Miner. Petrol. 154 (4), 429–437.
Fogliata, A.S., Báez, M.A., Hagemann, S.G., Santos, J.O., Sardi, F., 2012. Post-orogenic, Carboniferous granite-hosted Sn–W mineralization in the Sierras Pampeanas Orogen, Northwestern Argentina. Ore Geol. Rev. 45, 16–32.
Fu, B., Mernagh, T.P., Kita, N.T., Kemp, A.I., Valley, J.W., 2009. Distinguishing magmatic zircon from hydrothermal zircon: a case study from the Gidginbung high-sulphidation Au–Ag–(Cu) deposit, SE Australia. Chem. Geol. 259 (3–4), 131–142.
Gardiner, N.J., Hawkesworth, C.J., Robb, L.J., Whitehouse, M.J., Roberts, N.M., Kirkland, C.L., Evans, N.J., 2017. Contrasting granite metallogeny through the zircon record: a case study from Myanmar. Sci. Rep. 7 (1), 1–9.
Gebru, A.L., 2017. Petrogenesis of granitoids in the vicinity of the Mactung Tungsten Skarn Deposit, NE Yukon-Northwest Territories: characterization of skarn mineralization and causative plutons through geological, petrochemical, mineralogical, and geochronological analysis. University of New Brunswick. Doctoral dissertation.
Goldoff, B., Webster, J.D., Harlov, D.E., 2012. Characterization of fluor-chlorapatites by electron probe microanalysis with a focus on time-dependent intensity variation of halogens. Am. Mineral. 97, 1103–1115.
Guo, N.X., Zhao, Z., Gao, J.F., Chen, W., Wang, D.H., Chen, Y.C., 2018. Magmatic evolution and W-Sn-U-Nb-Ta mineralization of the Mesozoic Jiulongnao granitic complex, Nanling Range, South China. Ore Geol. Rev. 94, 414–434.
Guo, S., Chen, Y., Liu, C.Z., Wang, J.G., Su, B., Gao, Y.J., Wu, F.Y., Sein, K., Yang, Y.H., Mao, Q., 2016. Scheelite and coexisting F-rich zoned garnet, vesuvianite, fluorite, and apatite in calc-silicate rocks from the Mogok metamorphic belt, Myanmar: implications for metasomatism in marble and the role of halogens in W mobilization and mineralization. J. Asian Earth Sci. 117, 82–106.
Han, L., Huang, X.L., Li, J., He, P.L., Yao, J.M., 2016. Oxygen fugacity variation recorded in apatite of the granite in the Dahutang tungsten deposit, Jiangxi Province, South China. Acta Petrologica Sinica 32 (3), 746–758 in Chinese with English abstract.
Harlov, D.E., 2015. Apatite: a fingerprint for metasomatic processes. Elements 11 (3), 171–176.
Harrison, T.M., Watson, E.B., 1984. The behavior of apatite during crustal anatexis: equilibrium and kinetic considerations. Geochim. Cosmochim. Acta 48 (7), 1467–1477.
Harrison, T.M., Watson, E.B., Aikman, A.B., 2007. Temperature spectra of zircon crystallization in plutonic rocks. Geology 35, 635–638.
Hoskin, P.W., Schaltegger, U., 2003. The composition of zircon and igneous and metamorphic petrogenesis. Rev. Mineral. Geochem. 53 (1), 27–62.
Hoskin, P.W., 2005. Trace-element composition of hydrothermal zircon and the alteration of Hadean zircon from the Jack Hills, Australia. Geochim. Cosmochim. Acta 69 (3), 637–648.
Hua, R.M., Chen, P.R., Zhang, W.L., Lu, J.J., 2005. Three major metallogenic events in Mesozoic in South China. Mineral Deposits 24 (2), 99–107 in Chinese with English abstract.
Huang, L.C., Jiang, S.Y., 2014. Highly fractionated S-type granites from the giant Dahutang tungsten deposit in Jiangnan Orogen, Southeast China: geochronology, petrogenesis and their relationship with W-mineralization. Lithos 202–203, 207–226.
Huang, W., Wu, J., Liang, H., Zhang, J., Ren, L., Chen, X., 2020. Ages and genesis of W-Sn and Ta-Nb-Sn-W mineralization associated with the Limu granite complex, Guangxi, China. Lithos 352, 105321.
Hulsbosch, N., Boiron, M.C., Dewaele, S., Muchez, P., 2016. Fluid fractionation of tungsten during granite–pegmatite differentiation and the metal source of peribatholitic W quartz veins: evidence from the Karagwe-Ankole Belt (Rwanda). Geochim. Cosmochim. Acta 175, 299–318.
Jia, F., Zhang, C., Liu, H., Meng, X., Kong, Z., 2020. In situ major and trace element compositions of apatite from the Yangla skarn Cu deposit, southwest China: implications for petrogenesis and mineralization. Ore Geol. Rev. 127, 103360.
Jiang, S.Y., Zhao, K.D., Jiang, H., Su, H.M., Xiong, S.F., Xiong, Y.Q., Xu, Y.M., Zhang, W., Zhu, L.Y., 2020. Spatiotemporal distribution, geological characteristics and metallogenic mechanism of tungsten and tin deposits in China: an overview. Chin. Sci. Bull. 65 (33), 3730–3745.
Jiang, X.Y., Li, H., Ding, X., Wu, K., Guo, J., Liu, J.Q., Sun, W.D., 2018. Formation of A-type granites in the Lower Yangtze River Belt: a perspective from apatite geochemistry. Lithos 304, 125–134.
Kemp, A.I.S., Hawkesworth, C.J., Foster, G.L., Paterson, B.A., Woodhead, J.D., Hergt, J. M., Whitehouse, M.J., 2007. Magmatic and crustal differentiation history of granitic rocks from Hf–O isotopes in zircon. Science 315 (5814), 980–983.
Kempe, U., Wolf, D., 2006. Anomalously high Sc contents in ore minerals from Sn–W deposits: possible economic significance and genetic implications. Ore Geol. Rev. 28, 103–122.
Ketcham, R.A., 2015. Technical Note: Calculation of stoichiometry from EMP data for apatite and other phases with mixing on monovalent anion sites. Am. Mineral. 100, 1620–1623.
Kinny, P.D., Maas, R., 2003. Lu–Hf and Sm–Nd isotope systems in zircon. Rev. Mineral. Geochem. 53, 327–341.
Lecumberri-Sanchez, P., Vieira, R., Heinrich, C.A., Pinto, F., Wälle, M., 2017. Fluid-rock interaction is decisive for the formation of tungsten deposits. Geology 45 (7), 579–582.
Lehmann, B., 1990. The Metallogeny of Tin. Springer.
Lehmann, B., 2021. Formation of tin ore deposits: a reassessment. Lithos 402–403, 105756.
Lei, W.Y., Shi, G.H., Santosh, M., Ng, Y., Liu, Y.X., Wang, J., Xie, G., Ju, Y., 2016. Trace element features of hydrothermal and inherited igneous zircon grains in mantle wedge environment: a case study from the Myanmar jadeitite. Lithos 266, 16–27.
Li, J.Y., Wang, X.L., Zhang, F.F., Zhou, X.H., Shu, X.J., 2016. A rhythmic source change of the Neoproterozoic basement meta-sedimentary sequences in the Jiangnan Orogen: implications for tectonic evolution on the southeastern margin of the Yangtze Block. Precambr. Res. 280, 46–60.
Li, P., Yu, X., Li, H., Qiu, J., Zhou, X., 2013. Jurassic-Cretaceous tectonic evolution of Southeast China: geochronological and geochemical constraints of Yanshanian granitoids. Int. Geol. Rev. 55 (10), 1202–1219.
Li, Q.L., Li, X.H., Liu, Y., Tang, G.Q., Yang, J.H., Zhu, W.G., 2010. Precise U-Pb and Pb–Pb dating of Phanerozoic baddeleyite by SIMS with oxygen flooding technique. J. Anal. At. Spectrom. 25 (7), 1107–1113.
Li, W., Costa, F., 2020. A thermodynamic model for F-Cl-OH partitioning between silicate melts and apatite including non-ideal mixing with application to constraining melt volatile budgets. Geochim. Cosmochim. Acta 269, 203–222.
Li, W., Costa, F., Nagashima, K., 2021. Apatite crystals reveal melt volatile budgets and magma storage depths at Merapi volcano, Indonesia. J. Petrol. 62 (4), egaa100.
Li, X.H., Li, W.X., Li, Z.X., Lo, C.H., Wang, J., Ye, M.F., Yang, Y.H., 2009. Amalgamation between the Yangtze and Cathaysia Blocks in South China: constraints from SHRIMP U-Pb zircon ages, geochemistry and Nd–Hf isotopes of the Shuangxiwu volcanic rocks. Precambr. Res. 174, 117–128.
Li, X., Chi, G., Zhou, Y., Deng, T., Zhang, J., 2017. Oxygen fugacity of Yanshanian granites in South China and implications for metallogeny. Ore Geol. Rev. 88, 690–701.
Li, Y., Audétat, A., 2012. Partitioning of V, Mn Co, Ni, Cu, Zn, As, Mo, Ag, Sn, Sb, W, Au, Pb, and Bi between sulfide phases and hydrous basanite melt at upper mantle conditions. Earth Planet. Sci. Lett. 355, 327–340.
Liu, Y., Li, Q.L., Tang, G.Q., Li, X.H., Yin, Q.Z., 2015. Towards higher precision SIMS U–Pb zircon geochronology via dynamic multi-collector analysis. J. Anal. At. Spectrom. 30 (4), 979–985.
Loader, M.A., Wilkinson, J.J., Armstrong, R.N., 2017. The effect of titanite crystallisation on Eu and Ce anomalies in zircon and its implications for the assessment of porphyry Cu deposit fertility. Earth Planet. Sci. Lett. 472, 107–119.
Mao, J.W., Ouyang, H.G., Song, S.W., Santosh, M., Yuan, S.D., Zhou, Z.H., Zheng, W., Liu, H., Liu, P., Cheng, Y.B., Chen, M.H., 2019. Geology and metallogeny of tungsten and tin deposits in China. Soc. Econ. Geol. Special Publ. 22, 411–482.
Mao, J.W., Xie, G.Q., Guo, C.L., Chen, Y.C., 2007. Large-scale tungsten-tin mineralization in the Nanling region, South China: metallogenic ages and corresponding geodynamic processes. Acta Petrologica Sinica 23, 2329–2338 in Chinese with English abstract.
Mao, Z.H., Cheng, Y.B., Liu, J.J., Yuan, S.D., Wu, S.H., Xiang, X.K., Luo, X.H., 2013. Geology and molybdenite Re–Os age of the Dahutang granite-related veinlets-disseminated tungsten ore field in the Jiangxi Province, China. Ore Geol. Rev. 53, 422–433.
Marks, M.A., Wenzel, T., Whitehouse, M.J., Loose, M., Zack, T., Barth, M., Worgard, L., Krasz, V., Eby, G.N., Stosnach, H., Markl, G., 2012. The volatile inventory (F, Cl, Br, S, C) of magmatic apatite: An integrated analytical approach. Chem. Geol. 291, 241–255.
Mathez, E.A., Webster, J.D., 2005. Partitioning behavior of chlorine and fluorine in the system apatite-silicate melt-fluid. Geochim. Cosmochim. Acta 69 (5), 1275–1286.
Mengason, M.J., Candela, P.A., Piccoli, P.M., 2011. Molybdenum, tungsten and manganese partitioning in the system pyrrhotite–Fe–S–O melt–rhyolite melt: impact of sulfide segregation on arc magma evolution. Geochim. Cosmochim. Acta 75 (22), 7018–7030.
Miles, A.J., Graham, C.M., Hawkesworth, C.J., Gillespie, M.R., Hinton, R.W., Bromiley, G.D., 2014. Apatite: a new redox proxy for silicic magmas? Geochim. Cosmochim. Acta 132, 101–119.
Morton, A., Yaxley, G., 2007. Detrital apatite geochemistry and its application in provenance studies. Special Papers-Geol. Soc. Am. 420, 319–344.
Moss, R.L., Tzimas, E., Kara, H., Willis, P., Kooroshy, J., 2013. The potential risks from metals bottlenecks to the deployment of Strategic Energy Technologies. Energy Policy 55, 556–564.
Neiva, A.M.R., 2008. Geochemistry of cassiterite and wolframite from tin and tungsten quartz veins in Portugal. Ore Geol. Rev. 33, 221–238.
Pan, D.P., Wang, D., Wang, X.L., 2017. Petrogenesis of granites in Shimensi in northwestern Jiangxi Province and its implications for tungsten deposits. Geology in China 44 (1), 118–135 in Chinese with English abstract.
Pan, L.C., Hu, R.Z., Wang, X.S., Bi, X.W., Zhu, J.J., Li, C., 2016. Apatite trace element and halogen compositions as petrogenetic-metallogenic indicators: Examples from four granite plutons in the Sanjiang region, SW China. Lithos 254, 118–130.

Pyle, D.M., Mather, T.A., 2009. Halogens in igneous processes and their fluxes to the atmosphere and oceans from volcanic activity: a review. Chem. Geol. 263, 110–121.
Qi, H., Yang, X., Lu, S., Tang, C., Cao, J., Zhao, L., Lee, I., 2020. Ore genesis and fluid evolution of the Qiaomaishan Cu–W deposit, in the Middle-Lower Yangtze River Metallogenic Belt: evidence from in situ analyses of apatite and scheelite. Ore Geol. Rev. 127, 103864.
Qian, L., Wang, Y., Xie, J., Sun, W., 2019. The Late Mesozoic granodiorite and polymetallic mineralization in southern Anhui Province, China: a perspective from apatite geochemistry. Solid Earth Sci. 4 (4), 178–189.
Qiu, J.T., Yu, X.Q., Santosh, M., Zhang, D.H., Chen, S.Q., Li, P.J., 2013. Geochronology and magmatic oxygen fugacity of the Tongcun molybdenum deposit, northwest Zhejiang, SE China. Mineralium Deposita 48 (5), 545–556.
Rasmussen, K.L., Mortensen, J.K., 2013. Magmatic petrogenesis and the evolution of (F: Cl: OH) fluid composition in barren and tungsten skarn-associated plutons using apatite and biotite compositions: case studies from the northern Canadian Cordillera. Ore Geol. Rev. 50, 118–142.
René, M., Škoda, R., 2011. Nb-Ta-Ti oxides fractionation in rare-metal granites: Krásno-Horní Slavkov ore district, Czech Republic. Mineral. Petrol. 103 (1–4), 37–48.
Richards, J.P., 2009. Postsubduction porphyry Cu-Au and epithermal Au deposits: products of remelting of subduction-modified lithosphere. Geology 37 (3), 247–250.
Richards, J.P., 2015. The oxidation state, and sulfur and Cu contents of arc magmas: implications for metallogeny. Lithos 233, 27–45.
Rudnick, R.L., Gao, S., 2004. Composition of the continental crust. Treatise Geochem. 3, 1–64.
Schettler, G., Gottschalk, M., Harlov, D.E., 2011. A new semi-micro wet chemical method for apatite analysis and its application to the crystal chemistry of fluorapatite-chlorapatite solid solutions. Am. Mineral. 96 (1), 138–152.
Simons, B., Andersen, J.C., Shail, R.K., Jenner, F.E., 2017. Fractionation of Li, Be, Ga, Nb, Ta, In, Sn, Sb, W and Bi in the peraluminous Early Permian Variscan granites of the Cornubian Batholith: precursor processes to magmatic-hydrothermal mineralisation. Lithos 278, 491–512.
Smythe, D.J., Brenan, J.M., 2016. Magmatic oxygen fugacity estimated using zircon-melt partitioning of cerium. Earth Planet. Sci. Lett. 453, 260–266.
Song, S., Mao, J., Xie, G., Jian, W., Chen, G., Rao, J., Ouyang, Y., 2021. Petrogenesis of scheelite-bearing albitite as an indicator for the formation of a world-class scheelite skarn deposit: a case study of the Zhuxi Tungsten deposit. Econ. Geol. 116 (1), 91–121.
Song, S., Mao, J., Xie, G., Yao, Z., Chen, G., Rao, J., Ouyang, Y., 2018. The formation of the world-class Zhuxi scheelite skarn deposit: implications from the petrogenesis of scheelite-bearing anorthosite. Lithos 312, 153–170.
Stock, M.J., Humphreys, M.C.S., Smith, V.C., Johnson, R.D., Pyle, D.M., 2015. New constraints on electron-beam induced halogen migration in apatite. Am. Mineral. 100, 281–293.
Stormer, J., Pierson, M.L., Tacker, R.C., 1993. Variation of F and Cl X-ray intensity due to anisotropic diffusion in apatite. Am. Mineral. 78, 641–648.
Sun, K., Chen, B., Deng, J., Ma, X., 2018. Source of copper in the giant Shimensi W-Cu-Mo polymetallic deposit, South China: constraints from chalcopyrite geochemistry and oxygen fugacity of ore-related granites. Ore Geol. Rev. 101, 919–935.
Sun, W.D., Yang, X.Y., Fan, W.M., Wu, F.Y., 2012. Mesozoic large scale magmatism and mineralization in South China: preface. Lithos 150, 1–5.
Sun, W., Ding, X., Hu, Y.H., Li, X.H., 2007. The golden transformation of the Cretaceous plate subduction in the west Pacific. Earth Planet. Sci. Lett. 262 (3–4), 533–542.
Tang, M., Wang, X.L., Shu, X.J., Wang, D., Yang, T., Gopon, P., 2014. Hafnium isotopic heterogeneity in zircons from granitic rocks: Geochemical evaluation and modeling of "zircon effect" in crustal anatexis. Earth Planet. Sci. Lett. 389, 188–199.
Trail, D., Watson, E.B., Tailby, N.D., 2011. The oxidation state of Hadean magmas and implications for early Earth's atmosphere. Nature 480 (7375), 79–82.
Trail, D., Watson, E.B., Tailby, N.D., 2012. Ce and Eu anomalies in zircon as proxies for the oxidation state of magmas. Geochim. Cosmochim. Acta 97, 70–87.
Vigneresse, J.L., 2009. Evaluation of the chemical reactivity of the fluid phase through hard–soft acid–base concepts in magmatic intrusions with applications to ore generation. Chem. Geol. 158, 103–111.
Vonopartis, L.C., Kinnaird, J.A., Nex, P.A., Robb, L.J., 2021. African A-Type granites: A geochemical review on metallogenic potential. Lithos 396–397, 106229.
Wang, D., Wang, X.L., Cai, Y., Chen, X., Zhang, F.R., Zhang, F.F., 2017a. Heterogeneous conservation of zircon xenocrysts in late Jurassic granitic intrusions within the Neoproterozoic Jiuling Batholith, South China: a magma chamber growth model in deep crustal hot zones. J. Petrol. 58 (9), 1781–1810.
Wang, D., Wang, X.L., Zhou, J.C., Shu, X.J., 2013a. Unraveling the Precambrian crustal evolution by Neoproterozoic conglomerates, Jiangnan orogen: U-Pb and Hf isotopes of detrital zircons. Precambr. Res. 233, 223–236.
Wang, L.J., Griffin, W.L., Yu, J.H., O'Reilly, S.Y., 2012. Early crustal evolution in the western Yangtze Block: evidence from U-Pb and Lu–Hf isotopes on detrital zircons from sedimentary rocks. Precambr. Res. 222–223, 368–385.
Wang, R.C., Xie, L., Lu, J.J., Zhu, J.C., Chen, J., 2017b. Diversity of Mesozoic tin-bearing granites in the Nanling and adjacent regions, South China: Distinctive mineralogical patterns. Science China Earth Sciences 60 (11), 1909–1919.
Wang, W., Zhou, M.F., Yan, D.P., Li, L., Malpas, J., 2013b. Detrital zircon record of Neoproterozoic active-margin sedimentation in the eastern Jiangnan Orogen, South China. Precambr. Res. 235, 1–19.
Wang, X.L., Coble, M.A., Valley, J.W., Shu, X.J., Kitajima, K., Spicuzza, M.J., Sun, T., 2014a. Influence of radiation damage on Late Jurassic zircon from southern China: evidence from in situ measurements of oxygen isotopes, laser Raman, U-Pb ages, and trace elements. Chem. Geol. 389, 122–136.
Wang, X.L., Zhou, J.C., Griffin, W.L., Wang, R.C., Qiu, J.S., O'Reilly, S.Y., Xu, X.S., Liu, X. M., Zhang, G.L., 2007. Detrital zircon geochronology of Precambrian basement sequences in the Jiangnan orogen: dating the assembly of the Yangtze Cathaysia blocks. Precambr. Res. 159, 117–131.
Wang, X.L., Zhou, J.C., Griffin, W.L., Zhao, G.C., Yu, J.H., Qiu, J.S., Zhang, Y.J., Xing, G. F., 2014b. Geochemical Zonation across a Neoproterozoic Orogenic Belt: isotopic Evidence from Granitoids and Metasedimentary Rocks of the Jiangnan Orogen, China. Precambr. Res. 242, 154–171.
Watari, T., Nansai, K., Nakajima, K., 2020. Review of critical metal dynamics to 2050 for 48 elements. Resour. Conserv. Recycl. 155, 104669.
Watson, E.B., Harrison, T.M., 2005. Zircon thermometer reveals minimum melting conditions on earliest Earth. Science 308, 841–844.
Watson, E.B., Wark, D.A., Thomas, J.B., 2006. Crystallization thermometers for zircon and rutile. Contrib. Miner. Petrol. 151, 413–433.
Webster, J.D., Piccoli, P.M., 2015. Magmatic apatite: A powerful, yet deceptive, mineral. Elements 11 (3), 177–182.
Webster, J.D., Tappen, C.M., Mandeville, C.W., 2009. Partitioning behavior of chlorine and fluorine in the system apatite–melt–fluid. II: Felsic silicate systems at 200Mpa. Geochim. Cosmochim. Acta 73, 559–581.
Webster, J., Thomas, R., Förster, H.J., Seltmann, R., Tappen, C., 2004. Geochemical evolution of halogen-enriched granite magmas and mineralizing fluids of the Zinnwald tin-tungsten mining district, Erzgebirge, Germany. Miner. Deposita 39, 452–472.
Wei, W.F., Shen, N.P., Yan, B., Lai, C.K., Yang, J.H., Gao, W., Liang, F., 2018. Petrogenesis of ore-forming granites with implications for W-mineralization in the super-large Shimensi tungsten-dominated polymetallic deposit in northern Jiangxi Province, South China. Ore Geol. Rev. 95, 1123–1139.
White, L.T., Ireland, T.R., 2012. High-uranium matrix effect in zircon and its implications for SHRIMP U-Pb age determinations. Chem. Geol. 306, 78–91.
Wilson, G. A. & Eugster, H. (1990). Cassiterite solubility and tin speciation in supercritical chloride solution. In: Spencer, R.J., Chou, I. Ming (Eds.), Fluid-Mineral Interactions. A Tribute to H. P. Eugster. 2. Geochemical Society, Special Publication, 179–195.
Wood, S.A., Samson, I.M., 2000. The hydrothermal geochemistry of tungsten in granitoid environments: I. Relative solubilities of ferberite and scheelite as a function of T, P, pH and m(NaCl). Econ. Geol. Bull. Soc. Econ. Geol. 95, 143–182.
Xie, L., Liu, Y., Wang, R., Hu, H., Che, X., Xiang, L., 2019. Li–Nb–Ta mineralization in the Jurassic Yifeng granite-aplite intrusion within the Neoproterozoic Jiuling batholith, south China: a fluid-rich and quenching ore-forming process. J. Asian Earth Sci. 185, 104047.
Xie, L., Wang, Z., Wang, R., Zhu, J., Che, X., Gao, J., Zhao, X., 2018. Mineralogical constraints on the genesis of W–Nb–Ta mineralization in the Laiziling granite (Xianghualing district, South China). Ore Geol. Rev. 95, 695–712.
Xing, K., Shu, Q., Lentz, D.R., Wang, F., 2020. Zircon and apatite geochemical constraints on the formation of the Huojihe porphyry Mo deposit in the Lesser Xing'an Range, NE China. Am. Mineral. 105 (3), 382–396.
Xu, B., Jiang, S.Y., Wang, R., Ma, L., Zhao, K.D., Yan, X., 2015. Late Cretaceous granites from the giant Dulong Sn-polymetallic ore district in Yunnan Province, South China: geochronology, geochemistry, mineral chemistry and Nd–Hf isotopic compositions. Lithos 218, 54–72.
Yang, J.H., Kang, L.F., Peng, J.T., Zhong, H., Gao, J.F., Liu, L., 2018a. In-situ elemental and isotopic compositions of apatite and zircon from the Shuikoushan and Xihuashan granitic plutons: implication for Jurassic granitoid-related Cu-Pb-Zn and W mineralization in the Nanling Range, South China. Ore Geol. Rev. 93, 382–403.
Yang, Q., Xia, X., Zhang, W., Zhang, Y., Xiong, B., Xu, Y., Wei, G., 2018b. An evaluation of precision and accuracy of SIMS oxygen isotope analysis. Solid Earth Sci. 3 (3), 81–86.
Yao, J.L., Cawood, P.A., Shu, L.S., Zhao, G.C., 2019. Jiangnan Orogen, South China: A~970–820 Ma Rodinia margin accretionary belt. Earth Sci. Rev. 196, 102872.
Yao, J.L., Shu, L.S., Santosh, M., Li, J.Y., 2015. Neoproterozoic arc-related andesite and orogeny-related unconformity in the eastern Jiangnan orogenic belt: constraints on the assembly of the Yangtze and Cathaysia blocks in South China. Precambr. Res. 262, 84–100.
Yuan, S.D., Williams-Jones, A.E., Mao, J.W., Zhao, P.L., Yan, C., Zhang, D.L., 2018. The origin of the Zhangjialong tungsten deposit, South China: Implications for W-Sn mineralization in large granite batholiths. Econ. Geol. 113, 1193–1208.
Yuan, S.D., Williams-Jones, A.E., Romer, R.L., Zhao, P.L., Mao, J.W., 2019. Protolith-related thermal controls on the decoupling of Sn and W in Sn–W metallogenic provinces: Insights from the Nanling region. China. Economic Geol. 114 (5), 1005–1012.
Zafar, T., Leng, C.B., Zhang, X.C., Rehman, H.U., 2019. Geochemical attributes of magmatic apatite in the Kukaazi granite from western Kunlun orogenic belt, NW China: implications for granite petrogenesis and Pb-Zn (-Cu-W) mineralization. J. Geochem. Explor. 204, 256–269.
Zhang, W., Lentz, D.R., Thorne, K.G., McFarlane, C., 2016. Geochemical characteristics of biotite from felsic intrusive rocks around the Sisson Brook W-Mo–Cu deposit, west-central New Brunswick: an indicator of halogen and oxygen fugacity of magmatic systems. Ore Geol. Rev. 77, 82–96.
Zhang, Y., Ma, D.S., Gao, J.F., 2020. Origin and evolution of ore-forming fluids in a tungsten mineralization system, Middle Jiangnan orogenic belt, South China: constraints from in-situ LA–ICP–MS analyses of scheelite. Ore Geol. Rev. 127, 103806.
Zheng, Y.F., Zhang, S.B., Zhao, Z.F., Wu, Y.B., Li, X., Li, Z., Wu, F.Y., 2007. Contrasting zircon Hf and O isotopes in the two episodes of Neoproterozoic granitoids in South China: implications for growth and reworking of continental crust. Lithos 96 (1–2), 127–150.

Zhao, J.H., Zhou, M.F., Zheng, J.P., 2013. Constraints from zircon U-Pb ages, O and Hf isotopic compositions on the origin of Neoproterozoic peraluminous granitoids from the Jiangnan Fold Belt, South China. Contrib. Mineral. Petrol. 166, 1505–1519.
Zhao, P.L., Chu, X., Williams-Jones, A.E., Mao, J.W., Yuan, S.D., 2021. The role of phyllosilicate partial melting in segregating W and Sn deposits in W-Sn metallogenic provinces. Geology 50, 121–125.
Zhao, P.L., Zajacz, Z., Tsay, A., Yuan, S.D., 2022. Magmatic-hydrothermal tin deposits form in response to efficient tin extraction upon magma degassing. Geochim. Cosmochim. Acta 316, 331–346.
Zhao, W.W., Zhou, M.F., Li, Y.H.M., Zhao, Z., Gao, J.F., 2017. Genetic types, mineralization styles, and geodynamic settings of Mesozoic tungsten deposits in South China. J. Asian Earth Sci. 137, 109–140.
Zhong, S., Feng, C., Seltmann, R., Li, D., Dai, Z., 2018. Geochemical contrasts between Late Triassic ore-bearing and barren intrusions in the Weibao Cu–Pb–Zn deposit, East Kunlun Mountains, NW China: constraints from accessory minerals (zircon and apatite). Miner. Deposita 53 (6), 855–870.
Zhou, M.F., Gao, J.F., Zhao, Z., Zhao, W.W., 2018. Introduction to the special issue of Mesozoic W-Sn deposits in South China. Ore Geol. Rev. 101, 432–436.
Zhou, X.M., Sun, T., Shen, W.Z., Shu, L.S., Niu, Y.L., 2006. Petrogenesis of Mesozoic granitoids and volcanic rocks in South China: a response to tectonic evolution. Episodes 29, 26–33.
Zou, X., Qin, K., Han, X., Li, G., Evans, N.J., Li, Z., Yang, W., 2019. Insight into zircon REE oxy-barometers: a lattice strain model perspective. Earth Planet. Sci. Lett. 506, 87–96.